

Kitaev honeycomb antiferromagnet in a field: quantum phase diagram for general spin

Saeed S. Jahromi,^{1, 2, 3} Max Hörmann,⁴ Patrick Adelhardt,⁴
Sebastian Fey,⁴ Román Orús,^{1, 5, 3} and Kai Phillip Schmidt⁴

¹*Donostia International Physics Center, Paseo Manuel de Lardizabal 4, E-20018 San Sebastián, Spain*

²*Department of Physics, Institute for Advanced Studies in Basic Sciences (IASBS), Zanjan 45137-66731, Iran*

³*Multiverse Computing, Paseo de Miramón 170, E-20014 San Sebastián, Spain*

⁴*Lehrstuhl für Theoretische Physik I, Staudtstraße 7,*

FAU Erlangen-Nuremberg, D-91058 Erlangen, Germany

⁵*Ikerbasque Foundation for Science, Maria Diaz de Haro 3, E-48013 Bilbao, Spain*

We combine tensor-network approaches and high-order linked-cluster expansions to investigate the quantum phase diagram of the antiferromagnetic Kitaev's honeycomb model in a magnetic field for general spin values. For the pure Kitaev model, tensor network calculations confirm the absence of fluxes and spin-spin correlations beyond nearest neighbor in the ground state, but signal a breaking of the discrete orientational symmetry for $S \in \{1, 3/2, 2\}$ inline with the semiclassical limit. An intermediate region between Kitaev phases and the high-field polarized phase is demonstrated for all considered spin values. The analysis of the high-field gap and the associated spectral weight of the polarized phase for general spin S is consistent with an unconventional quantum critical breakdown of the high-field polarized phase in accordance with the presence of exotic physics at intermediate Kitaev couplings.

Introduction.- Quantum spin liquids (QSLs) are exotic phases of matter which remain disordered for all temperatures and host a variety of fascinating physical properties such as, emergent gauge structures [1, 2]. This includes two- and three-dimensional gapped QSLs with intrinsic topological order displaying highly entangled ground states and unconventional anyonic statistics [3–8], which are at the heart of topological quantum computation [9–12], as well as 3d fracton topological order [13–15], whose robustness is believed to be relevant for topologically protected quantum memories. In contrast, their gapless counterparts display distinct prominent features like emergent (3+1)d quantum electrodynamics in the Coulomb QSL [16–18], but also algebraic Dirac spin liquids [19–22] as well as spin-Bose metals exist in several 2d frustrated quantum magnets [23–26].

Kitaev's honeycomb model [9] is one of the most prominent systems in this context, since its spin-1/2 version is exactly solvable in terms of Majorana fermions and realizes gapped and gapless \mathbb{Z}_2 QSLs in the ground-state phase diagram. This QSL originates from frustrated bond-dependent Ising interactions. The fate of the gapless Kitaev QSL in the presence of a field along the (1,1,1)-direction is qualitatively different for ferro- and antiferromagnetic Kitaev interactions [28, 29, 31]. In the ferromagnetic case, numerical investigations for isotropic Kitaev couplings consistently show a direct transition between the gapped Kitaev QSL with non-Abelian topological order at finite fields and the high-field polarized phase. In contrast, for antiferromagnetic Kitaev interactions, several numerical approaches show the presence of an intermediate phase [28, 29, 31, 32]. This intermediate phase is claimed to be a gapless QSL with an emergent U(1) gauge structure and therefore (2+1)d quantum electrodynamics [31]. Furthermore, calculations based on exact diagonalization (ED) [32, 33], density matrix

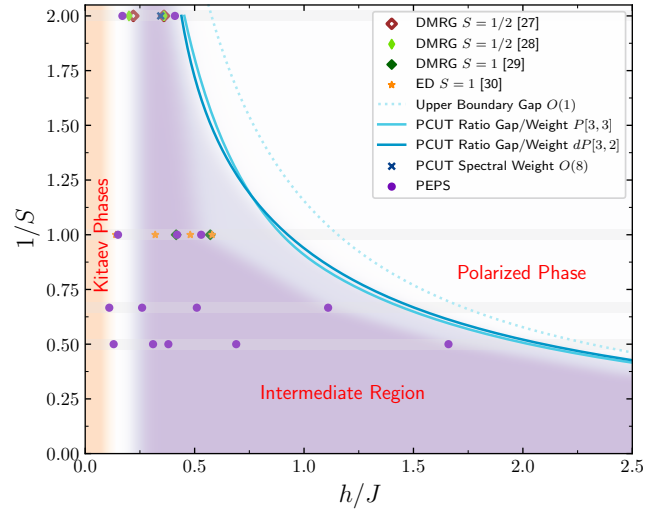


FIG. 1. (Color online) Phase diagram of the antiferromagnetic spin- S Kitaev's honeycomb model in a (1,1,1)-field as a function of h/J and $1/S$. Filled circles correspond to iPEPS data while lines originate from the high-field PCUT expansion. Solid lines correspond to Padé (DlogPadé) approximant $P[L, M]$ ($dP[L, M]$) [27] of the ratio gap Δ^S over spectral weight A_{Gap}^S (see below) from PCUTs. The DMRG and ED benchmark data were obtained from Refs. [28–30] and [31], respectively.

renormalization group (DMRG) [30], and tensor networks (TN) [34] indicate the presence of a similar intermediate region for the antiferromagnetic spin-one Kitaev model in a field.

The presence of an intermediate region for $S \in \{1/2, 1\}$ immediately calls for an investigation of the antiferromagnetic Kitaev model in a field for general spin values

S. Indeed, it was conjectured that an intermediate U(1) QSL is present for all S and that the phase transition between the two QSLs at low and intermediate fields is given by an Anderson-Higgs transition [32, 35]. At the same time the phase transition between the high-field polarized phase and the intermediate Kitaev region is only poorly understood. In this paper, we gain further insights in the ground-state phase diagram for general S by applying complementary TN approaches as well as linked-cluster expansions in the thermodynamic limit.

Model.— We study the Kitaev’s honeycomb model in a uniform magnetic field along the (1,1,1)-direction, so that the Hamiltonian reads

$$\mathcal{H}_{\text{KIF}} = J \sum_{\substack{\alpha-\text{links} \\ \alpha=x,y,z \\ < i,j >}} S_i^\alpha S_j^\alpha + h \sum_i (S_i^x + S_i^y + S_i^z), \quad (1)$$

where S_i^α are spin- S operators with $[S_i^\alpha, S_j^\beta] = i\epsilon_{\alpha\beta\gamma} S_i^\gamma$, $J > 0$ (antiferromagnetic), and we choose h to be positive. The pure Kitaev model for $h = 0$ has a conserved quantum number per plaquette p for general S given by the eigenvalues ± 1 of the plaquette operators $W_p = -e^{i\pi(S_1^x + S_2^y + S_3^z + S_4^x + S_5^y + S_6^z)}$, which is the basis for the exact solution for $S = 1/2$ yielding a flux-free (i.e., $W_p = +1$ for all p) and a gapless QSL ground state [9]. For $S > 1/2$, the system is not exactly solvable anymore, but it is known that even in the classical limit, the pure Kitaev model does not order magnetically due to the strong frustration [36]. In the semi-classical limit, the ground state remains flux free but it is a gapped \mathbb{Z}_2 QSL with vanishing spin-spin correlations beyond nearest-neighbors and a breaking of orientational symmetry [37, 38]. The semi-classical approximation is expected to hold for $S \gtrsim 3/2$. Moreover, DMRG calculations for $S = 1$ [30] and $S = 3/2$ [39] predict a gapless QSL ground state similar to $S = 1/2$ while TN calculations [34] predict a gapped QSL for $S = 1$ inline with the semi-classical findings [38]. For finite fields $h > 0$ and $S \in \{1/2, 1\}$ there is convincing evidence by ED [31–33] and DMRG [28–30] for the presence of an intermediate region in the phase diagram between the gapped Kitaev phase at small (but finite) fields and the high-field polarized phase, which is also gapped but topologically trivial.

Tensor-Network methods.— Tensor-Network (TN) methods [40–45] provide efficient representations for ground states of local Hamiltonians based on their entanglement structure [40]. In particular, the projected entangled-pair state (PEPS) method and its infinite version in the thermodynamic limit (iPEPS) [40, 41, 45, 46], have played a major role in the characterization and discovery of many exotic phases, ranging from magnetically ordered states [47–49] to QSLs [19, 21, 50, 51] and valence-bond crystals [52, 53]. In particular, the modified version of the iPEPS algorithm, designed for the honeycomb structures [54], has been shown to be very successful for simulating and characterizing the Kitaev

model and its variants, such as the Kitaev-Heisenberg model, in the thermodynamic limit [55–57].

In this study we use three variants of the iPEPS algorithm based on simple update (SU) [57–59], full update (FU) [49, 53, 60, 61], and a more recent graph-based PEPS algorithm (gPEPS) [57], in order to simulate the Kitaev model in the presence of a uniform magnetic field for generic spin- S values. While both SU and gPEPS algorithms use mean-field-like environment and local tensor updates based on singular-value decomposition, the FU takes the full environment into account and captures the full correlations around local tensors. The FU algorithm is therefore computationally more expensive. We simulated the Kitaev model for different S on different unit-cells with 8, 12, 16 and 32 sites and different bond dimensions D . The maximum achievable dimensions were $D = 6, 12$ and 18 for FU, SU and gPEPS simulations, respectively. Our optimization algorithms in all aforementioned approaches was based on imaginary-time evolution [40, 62] with $\delta\tau$ starting from 10^{-1} down to 10^{-5} with 4000 maximum iterations to ensure both convergence and accuracy.

Let us further note that we used the corner transfer matrix renormalization group (CTMRG) method [47, 59, 61, 63] for contracting the 2D infinite TN in the FU algorithm as well as for calculating the variational energies and expectation values of local operators in both SU and FU. The maximum affordable boundary dimension χ was 40 and 60 for FU and SU simulations, respectively. Moreover, we used the mean-field-like environment for calculating the expectation values in the gPEPS technique, thus allowing for a larger achievable bond dimension D [57]. However, one should note that by using the mean-field environments the correlations beyond the nearest neighbors are captured less accurately and the expectation values are no-longer variational. Please see the supplementary material [27] for details of the algorithms and their implementation.

Linked-cluster expansions.— The method of perturbative continuous unitary transformations (pCUTs) [64, 65] maps the Hamiltonian (1) for a general spin value S unitarily to an effective Hamiltonian \mathcal{H}_{eff} , which conserves the number of quasi-particles (qp) in the polarized high-field phase where spins point in (1,1,1)-direction. This mapping is done perturbatively up to high orders in powers of J/h . The quasi-particles in the polarized phase correspond to dressed spin-flip excitations, which are adiabatically connected to localized spin flips above the fully polarized state $|\text{ref}\rangle \equiv | -S - S \dots - S \rangle$ in the limit $h \rightarrow \infty$. We take the field term as the unperturbed part \mathcal{H}_0 , which has an equidistant spectrum for any spin value S . The Kitaev interactions then correspond to the perturbation changing the number of spin flips by $N \in \{0, \pm 1, \pm 2\}$. Employing a white-graph expansion [66, 67] we performed pCUT calculations in the 0qp and 1qp sector either for fixed spin $S \in \{1/2, 1\}$ or by keeping the spin S as a general variable. This allows

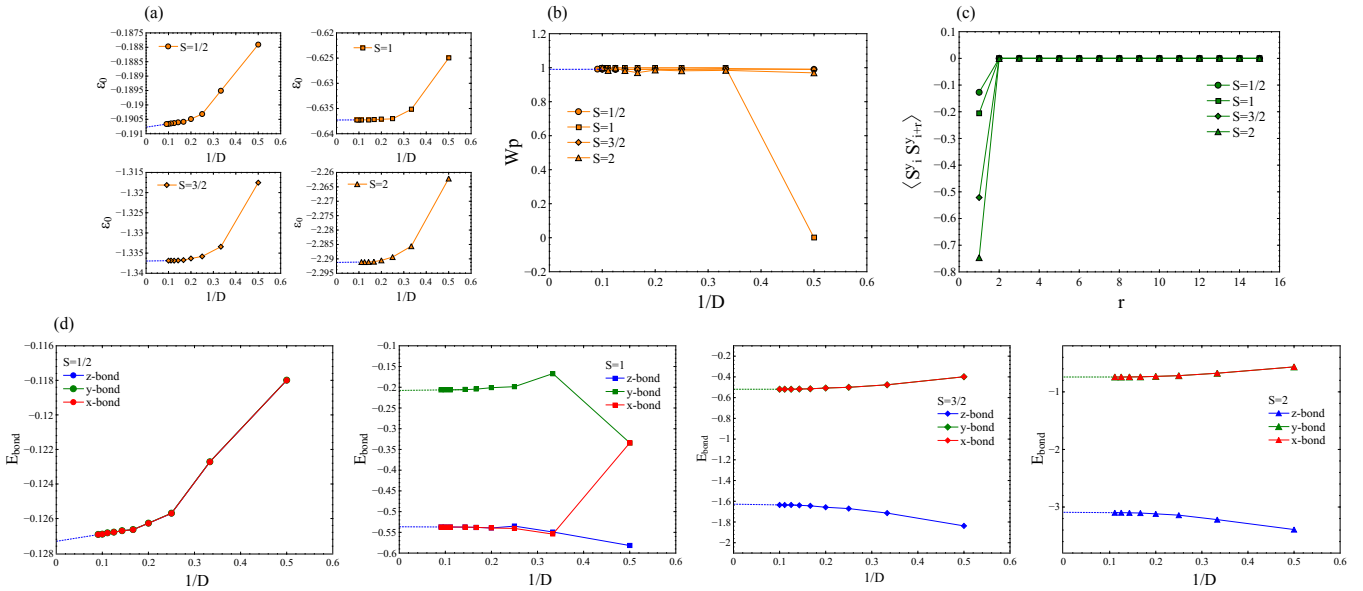


FIG. 2. (Color online) TN results for the pure spin- S Kitaev model with $S \in \{1/2, 1, 3/2, 2\}$: (a) Ground-state energy per-site, ε_0 , obtained from iPEPS with SU algorithm. (b) Plaquette operator W_p . (c) Spin-spin correlation functions $\langle S_i^y S_{i+r}^y \rangle$, where r is the distance from a green link along the zigzag chain connected to that link and (d) Bond energy $E_{\text{bond}} = J_\alpha \langle S_i^\alpha S_{i+1}^\alpha \rangle$ (α -links) as a function of $1/D$. For the other spin flavors we found identical results.

us to determine the ground-state energy per site ε_0^S (order 9 for $S = 1/2$, order 8 for $S = 1$, and order 7 for general S) and the one-quasi-particle gap Δ^S (order 9 for $S = 1/2$, order 8 for $S = 1$, and order 7 for general S) as a high-order polynomial in J/h and S . The 1qp sector consists of two 1qp bands $\omega^S(\vec{k}, n)$ with \vec{k} the momentum and $n \in \{\text{low, high}\}$ the band index due to the two-site unit cell. The gap Δ^S is the minimum of the lower 1qp band $\omega(\vec{k}, \text{low})$ located at the gap momentum $\vec{k} = \vec{0}$ for all S .

Furthermore, we used the pCUT method to calculate the 1qp spectral weight $A_{\text{Gap}}^S \equiv |\langle \text{ref} | \mathcal{O}_{\text{Gap}}^{\text{eff}} | \Delta^S \rangle|^2$ of the gap mode $|\Delta^S\rangle$. $\mathcal{O}_{\text{Gap}}^{\text{eff}}$ is the superposition of the local observable $\mathcal{O}_i^{\text{eff}}$, which results from the unitary transformation of $\mathcal{O}_i = S_i^z$, with same phase factors as the gap mode. We calculated order 8 for $S = 1/2$ and order 6 for general S . The explicit series of all calculated quantities are given in the supplementary materials [27].

Phase diagram.— Our major findings are summarized in Fig. 1, where we show the computed ground-state phase diagram of the antiferromagnetic spin- S Kitaev’s honeycomb model in a (1,1,1)-field as a function of h/J and $1/S$. The results are based on TN calculations for $S \in \{1/2, 1, 3/2, 2\}$ and high-order series expansions for general S in the high-field polarized phase.

The TN results for the pure Kitaev model $h = 0$ and $S \leq 2$ are shown in Fig. 2. Our estimated ground-state energy per-site, ε_0 , obtained from $D = 11$ iPEPS simulations with SU algorithm, are $\varepsilon_0 \in \{-0.19077, -0.63727, -1.33696, -2.29122\}$ for $S \in \{1/2, 1, 3/2, 2\}$, respectively. Moreover, we find in

all cases a flux-free ground state with vanishing spin-spin correlations beyond nearest neighbor, in turn consistent with earlier findings. In addition, for $S = 1/2$, the bond energies are fully symmetric on x , y , and z bonds, also in agreement with the exact gapless QSL ground state. In contrast, in all other cases the bond energies are anisotropic and the convergence with $1/D$ is faster, pointing to a gapped QSL in agreement with the semi-classical limit [38] and earlier TN calculations for $S = 1$ [34]. Except for the $S = 1/2$ case, where a finite field is necessary to open an energy gap, the ground state for small but finite field is adiabatically connected to the pure Kitaev model and can therefore be characterized similarly. In the phase diagram in Fig. 1, this region is coined as a Kitaev phase, and extends for all considered spin values until $h/J \approx 0.15$. Our TN analysis for the pure Kitaev limit further points towards vanishing magnetization as a function of $1/D$ for all spin values S . Besides, the anisotropic bond energies on the x , y , and z links for $S > 1/2$ form degenerate patterns with two of the bonds having the same energies while the third one being considerably different, i.e., forming dimerized patterns on the honeycomb lattice consistent with the semi-classical limit [38]. Moving slightly away from the isotropic point, e.g., $(J_x = 1.1, J_y = 0.95, J_z = 0.95)$, we find that the bond with larger exchange coupling always has lower energy (see supplementary material [27]). Let us further note that similar remarks hold as well for the pure ferromagnetic Kitaev model for all considered spin S (not shown here).

For $h/J \gtrsim 0.15$, we find an intermediate regime for all S which increases in size when increasing S (see Fig. 1).

As shown in Fig. 3, the phase boundaries can be

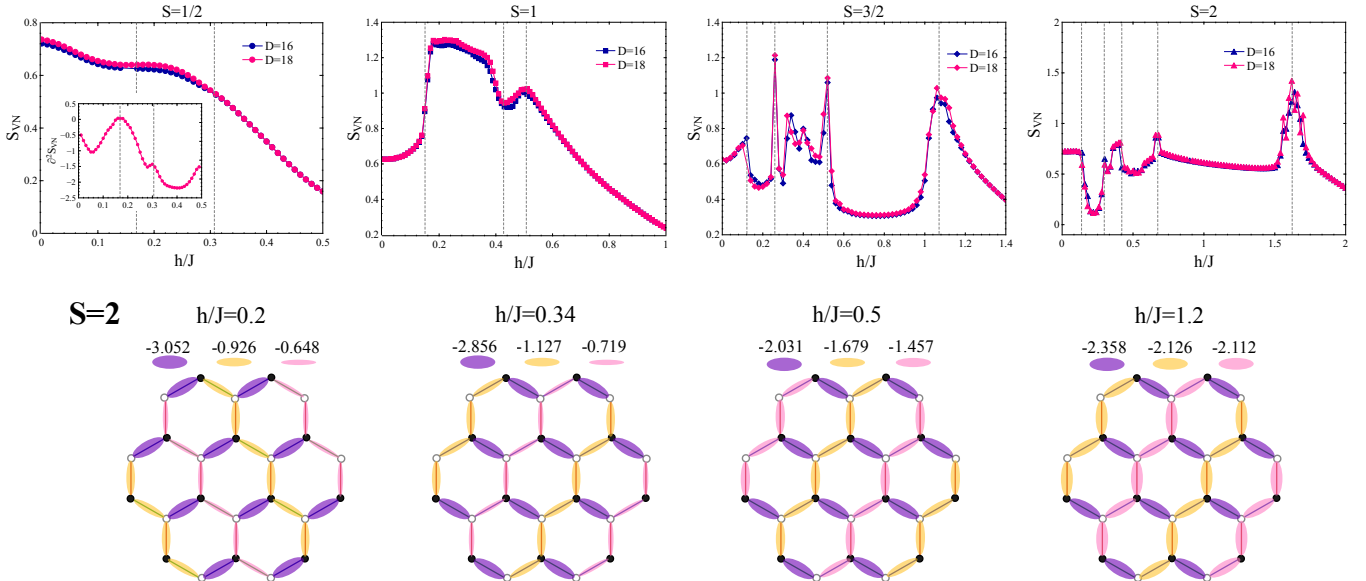


FIG. 3. (Color online) (Upper panel) TN results for the bond-entanglement entropy S_{VN} (see text for definition) as a function of h/J for $S = 1/2$ (left), $S = 1$ (middle left), $S = 3/2$ (middle right), and $S = 2$ (right). (Lower panel) Configurations of bond energies in the sub-regions of the intermediate phase for $S = 2$.

well detected by the bond-entanglement entropy $S_{VN} = -\sum_i \lambda_i \log_2(\lambda_i)$ where λ_i 's are the singular values obtained from local singular-value decomposition in the process of the simple-update. For each S , we observe several phase boundaries. The first and last boundaries separate the Kitaev and polarized phases from the intermediate region, whereas the rest can be considered as different variants of the same phase. In order to shed light on the nature of the intermediate sub-regions, let us remind of the anisotropic bond energies in the pure Kitaev limit for $S > 1/2$. Our TN analysis shows that the anisotropic bond energies continue to persist in the intermediate regime as well. Measuring bond energies deep inside each sub-region, we find that they have different strong-weak bond patterns which are, however, all related by symmetry (see Fig. 3-lower panel for $S = 2$). These $2S$ sub-regions with different (symmetry-related) local configurations suggest that they all belong to the same phase between the Kitaev phase in the small-field limit and the polarized phase at large fields. Let us further stress that similar weak features have already been observed in ED simulations for $S \in \{1/2, 1\}$ [31, 32].

Finally, we discuss the breakdown of the high-field polarized phase towards the intermediate region. Our corresponding results for the 1qp gap Δ^S and the 1qp spectral weight A_{Gap}^S are shown in Fig. 4. We expect the gap Δ^S to close at the quantum critical point J_{crit} . We note, however, that a potential first-order phase transition for $J < J_{\text{crit}}$ can not be detected with the gap series, but is absent in our TN calculations. Also, existing DMRG data [28–30] points towards a continuous phase transition. For increasing S , the gap closes for smaller values of J_{crit} so that the polarized phase is re-

duced (see also Fig. 1). Interestingly, the breakdown of the polarized phase is found at rather large values of J_{crit} by TN and DMRG calculations implying that Δ^S closes very flat as a function of J , i.e., $\Delta^S \propto (J - J_{\text{crit}})^{z\nu}$ with critical exponent $z\nu$ substantially larger than one. For $S = 1/2$, this can be also seen in the dynamic structure factor calculated by DMRG [28]. This peculiar behavior is likely also the reason why conventional extrapolation techniques like Padé and Dlog Padé approximation [27, 68] do not work for the Δ^S (see Ref. [69] for similar findings) and we restrict the discussion mostly to the bare series. The 1qp spectral weight A_{Gap}^S behaves opposite to the gap in the sense that higher perturbative orders become less important compared to the zeroth order $2S$. As a consequence, while our series data is consistent for a vanishing 1qp spectral weight at J_{crit} for $S = 1/2$, the spectral weight remains finite in the whole polarized phase for $S > 1/2$. Interestingly, the ratio $\Delta^S/A_{\text{Gap}}^S$ allows a consistent extrapolation for all S . Corresponding Padé and Dlog Padé approximants are displayed in Fig. 1 as solid phase transition lines and show convincing agreement with our TN results. Overall, also our series-expansion results display the difference between $S = 1/2$ and $S > 1/2$ consistent with the findings from TN.

Conclusions and outlook.— We applied TN approaches and linked-cluster expansions to investigate the ground-state phase diagram of the antiferromagnetic Kitaev's honeycomb model in a (1,1,1)-field for general spin values. While an intermediate region between the low-field Kitaev and the high-field polarized phase is found for all studied S consistent with the literature, our results show distinct behavior for $S = 1/2$ and $S > 1/2$. For the Kitaev phase, our TN calculations confirm the ab-

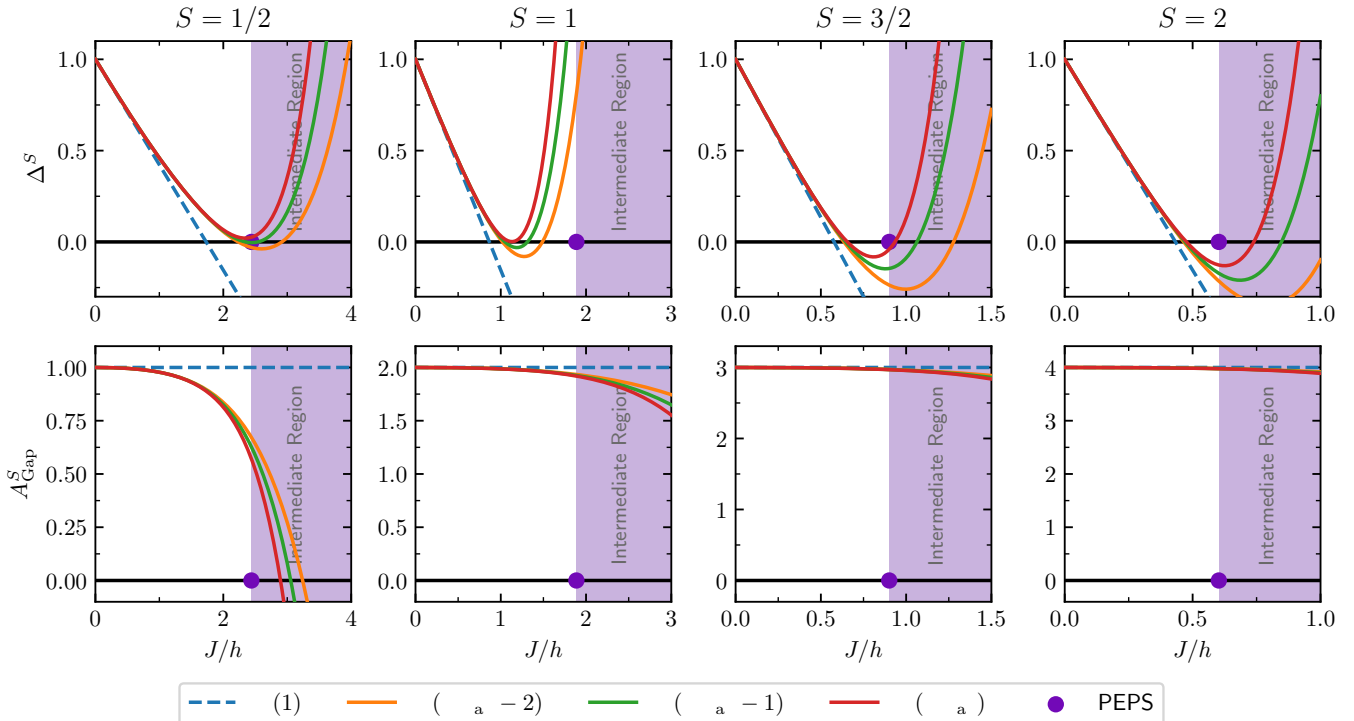


FIG. 4. (Color online) pCUT results for the 1qp gap Δ^S (upper panel) and the 1qp spectral weight A_{Gap}^S (lower panel) of the high-field polarized phase as a function of J/h for $S = 1/2$ (left), $S = 1$ (middle left), $S = 3/2$ (middle right), and $S = 2$ (right). Dashed lines correspond to the first-order results while solid lines represent the three highest perturbative orders for each quantity (O_{max} denotes the maximal order reached). Purple circles and shaded regions illustrated the phase transition points and the intermediate regions as obtained from the iPEPS calculations.

sence of fluxes and spin-spin correlations beyond nearest neighbor in the ground state, but signal a breaking of the discrete orientational symmetry for $S \in \{1, 3/2, 2\}$ inline with the semiclassical limit which can be clearly seen in the anisotropies of bond energies. For the high-field polarized phase, the analysis of the gap indicates an unconventional quantum critical breakdown for all S in accordance with the presence of exotic physics at intermediate Kitaev couplings. Again, a difference between $S = 1/2$ and $S > 1/2$ can be seen in the associated spectral weights.

Antiferromagnetic Kitaev models in finite magnetic fields represent therefore an exciting and challenging

playground for general values of S . A deeper understanding of the intermediate region as well as of the quantum critical behavior is certainly still needed. This includes also the generalization to arbitrary field directions and anisotropic Kitaev couplings.

Acknowledgments.— We thank S. Trebst for fruitful discussion. M. Gohlke and F. Pollmann for providing DMRG data. The TN simulations were performed on ATLAS HPC cluster at DIPC. KPS acknowledges financial support by the German Science Foundation (DFG) through the grant SCHM 2511/11-1. RO and SSJ acknowledge financial support from Ikerbasque and DIPC.

[1] L. Balents, *Nature* **464**, 199 (2010), arXiv:9904169 [cond-mat].

[2] L. Savary and L. Balents, *Reports on Progress in Physics* **80**, 016502 (2017).

[3] J. M. Leinaas and J. Myrheim, *Nuovo Cimento Soc. Ital. Fis., B* **37**, 1 (1977).

[4] F. Wilczek, *Phys. Rev. Lett.* **48**, 1144 (1982).

[5] M. Levin and X. G. Wen, *Physical Review Letters* **96**, 110405 (2006), arXiv:0510613 [cond-mat].

[6] S. S. Jahromi and A. Langari, *Journal of Physics A: Mathematical and Theoretical* **50**, 145305 (2017), arXiv:1512.00756.

[7] S. Capponi, S. S. Jahromi, F. Alet, and K. P. Schmidt, *Physical Review E - Statistical, Nonlinear, and Soft Matter Physics* **89**, 062136 (2014), arXiv:1403.1406.

[8] S. S. Jahromi, M. Kargarian, S. F. Masoudi, and A. Langari, *Physical Review B* **94**, 125145 (2016), arXiv:1608.00254.

[9] A. Kitaev, *Annals of Physics* **321**, 2 (2006), arXiv:0506438 [cond-mat].

[10] C. Nayak, S. H. Simon, A. Stern, M. Freedman, and S. Das Sarma, *Reviews of Modern Physics* **80**, 1083 (2008), arXiv:0707.1889.

[11] A. Kitaev, *Annals of Physics* **303**, 2 (2003).

[12] M. A. Levin and X. G. Wen, *Physical Review B - Condensed Matter and Materials Physics* **71**, 045110 (2005), arXiv:0404617 [cond-mat].

[13] C. Chamon, *Phys. Rev. Lett.* **94**, 40402 (2005).

[14] S. Bravyi, B. Leemhuis, and B. M. Terhal, *Ann. Phys.* **326**, 839 (2011).

[15] J. Haah, *Phys. Rev. A* **83**, 42330 (2011).

[16] M. Hermele, M. P. A. Fisher, and L. Balents, *Phys. Rev. B* **69**, 064404 (2004).

[17] N. Shannon, O. Sikora, F. Pollmann, K. Penc, and P. Fulde, *Phys. Rev. Lett.* **108**, 067204 (2012).

[18] J. Röchner, L. Balents, and K. P. Schmidt, *Phys. Rev. B* **94**, 201111 (2016).

[19] T. Picot, M. Ziegler, R. Orús, and D. Poilblanc, *Physical Review B* **93**, 060407 (2016).

[20] H. J. Liao, Z. Y. Xie, J. Chen, Z. Y. Liu, H. D. Xie, R. Z. Huang, B. Normand, and T. Xiang, *Physical Review Letters* **118**, 137202 (2017), arXiv:1610.04727.

[21] Z. Y. Xie, J. Chen, J. F. Yu, X. Kong, B. Normand, and T. Xiang, *Physical Review X* **4**, 011025 (2014), arXiv:1307.5696.

[22] Y.-C. He, M. P. Zaletel, M. Oshikawa, and F. Pollmann, *Physical Review X* **7**, 031020 (2017).

[23] O. I. Motrunich, *Phys. Rev. B* **72**, 045105 (2005).

[24] S.-S. Lee and P. A. Lee, *Phys. Rev. Lett.* **95**, 036403 (2005).

[25] D. N. Sheng, O. I. Motrunich, and M. P. A. Fisher, *Phys. Rev. B* **79**, 205112 (2009).

[26] H.-Y. Yang, A. M. Läuchli, F. Mila, and K. P. Schmidt, *Phys. Rev. Lett.* **105**, 267204 (2010).

[27] See supplementary materials for details of the tensor network algorithm as well as of the pCUT method including the explicit series expressions for fixed S and arbitrary S and some information on the extrapolation..

[28] M. Gohlke, R. Moessner, and F. Pollmann, *Phys. Rev. B* **98**, 144148 (2018).

[29] Z. Zhu, I. Kimchi, D. N. Sheng, and L. Fu, *Phys. Rev. B* **97**, 241110 (2018).

[30] Z. Zhu, Z.-Y. Weng, and D. N. Sheng, *Phys. Rev. Research* **2**, 22047 (2020).

[31] C. Hickey and S. Trebst, *Nature Communications* **10**, 530 (2019).

[32] C. Hickey, C. Berke, P. P. Stavropoulos, H.-Y. Kee, and S. Trebst, *Phys. Rev. Research* **2**, 23361 (2020).

[33] C. Hickey, M. Gohlke, C. Berke, and S. Trebst, *Phys. Rev. B* **103**, 64417 (2021).

[34] H.-Y. Lee, N. Kawashima, and Y. B. Kim, *Phys. Rev. Res.* **2** (2020), 10.1103/physrevresearch.2.033318, arXiv:1911.07714.

[35] S.-S. Zhang, G. B. Halász, and C. D. Batista, “Theory of the Kitaev model in a [111] magnetic field,” (2021), arXiv:2104.02892 [cond-mat.str-el].

[36] G. Baskaran, S. Mandal, and R. Shankar, *Physical Review Letters* **98**, 247201 (2007), arXiv:0611547 [cond-mat].

[37] G. Baskaran, D. Sen, and R. Shankar, *Phys. Rev. B - Condens. Matter Mater. Phys.* **78**, 1 (2008), arXiv:0806.1588.

[38] I. Rousochatzakis, Y. Sizyuk, and N. B. Perkins, *Nature Communications* **9**, 1575 (2018).

[39] H.-K. Jin, W. M. H. Natori, F. Pollmann, and J. Knolle, “Unveiling the $S=3/2$ Kitaev Honeycomb Spin Liquids,” (2021), arXiv:2107.13364 [cond-mat.str-el].

[40] R. Orús, *Annals of Physics* **349**, 117 (2014), arXiv:1306.2164.

[41] R. Orús, *European Physical Journal B* **87**, 280 (2014), arXiv:1407.6552.

[42] R. Orús, *Nature Reviews Physics* **1**, 538 (2019).

[43] S.-J. Ran, E. Tirrito, C. Peng, X. Chen, G. Su, and M. Lewenstein, (2017), 10.1016/j.hrmr.2011.11.009, arXiv:1708.09213.

[44] J. Biamonte and V. Bergholm, (2017), arXiv:1708.00006.

[45] F. Verstraete, V. Murg, and J. I. Cirac, *Advances in Physics* **57**, 143 (2008), arXiv:0907.2796.

[46] F. Verstraete, M. M. Wolf, D. Perez-Garcia, and J. I. Cirac, *Physical Review Letters* **96**, 220601 (2006), arXiv:0601075 [quant-ph].

[47] R. Orús and G. Vidal, *Physical Review B - Condensed Matter and Materials Physics* **80**, 094403 (2009), arXiv:0905.3225.

[48] P. Corboz and F. Mila, *Physical Review B - Condensed Matter and Materials Physics* **87**, 115144 (2013), arXiv:arXiv:1212.2983v2.

[49] H. N. Phien, J. A. Bengua, H. D. Tuan, P. Corboz, and R. Orús, *Physical Review B - Condensed Matter and Materials Physics* **92**, 035142 (2015), arXiv:1503.05345.

[50] S. S. Jahromi, H. Yarloo, and R. Orús, *Physical Review Research* **3**, 033205 (2021).

[51] S. S. Jahromi and R. Orús, *Physical Review B* **101**, 115114 (2020).

[52] Y. Iqbal, D. Poilblanc, R. Thomale, and F. Becca, *Physical Review B* **97**, 115127 (2018).

[53] S. S. Jahromi and R. Orús, *Physical Review B* **98**, 155108 (2018).

[54] S. S. Jahromi, R. Orús, M. Kargarian, and A. Langari, *Physical Review B* **97**, 115161 (2018).

[55] J. Osorio Iregui, P. Corboz, and M. Troyer, *Physical Review B - Condensed Matter and Materials Physics* **90**, 195102 (2014), arXiv:1408.4020.

[56] P. Czarnik, A. Francuz, and J. Dziarmaga, *Physical Review B* **100**, 165147 (2019), arXiv:1906.02220.

[57] S. S. Jahromi and R. Orús, *Physical Review B* **99**, 195105 (2019).

[58] H. C. Jiang, Z. Y. Weng, and T. Xiang, *Physical Review Letters* **101**, 090603 (2008), arXiv:0806.3719.

[59] P. Corboz, J. Jordan, and G. Vidal, *Physical Review B - Condensed Matter and Materials Physics* **82**, 245119 (2010), arXiv:1008.3937.

[60] P. Corboz and F. Mila, *Physical Review Letters* **112**, 147203 (2014), arXiv:arXiv:1401.3778v1.

[61] P. Corboz, T. M. Rice, and M. Troyer, *Physical Review Letters* **113**, 046402 (2014), arXiv:1402.2859.

[62] R. Orús and G. Vidal, *Physical Review B - Condensed Matter and Materials Physics* **78**, 155117 (2008), arXiv:0711.3960.

[63] T. Nishino and K. Okunishi, *Journal of the Physical Society of Japan* **65**, 891 (1996), arXiv:9507087 [cond-mat].

[64] C. Knetter and G. S. Uhrig, *The European Physical Journal B* **225**, 209 (2000), arXiv:9906243v1 [arXiv:cond-mat].

[65] C. Knetter, K. P. Schmidt, and G. S. Uhrig, *Journal of Physics A: Mathematical and General* **36**, 7889 (2003), arXiv:0306333 [cond-mat].

[66] K. Coester and K. P. Schmidt, *Physical Review E* **92**,

22118 (2015).

[67] P. Adelhardt, J. A. Koziol, A. Schellenberger, and K. P. Schmidt, [Phys. Rev. B](#) **102**, 174424 (2020).

[68] A. C. Guttmann, *Phase Transitions and Critical Phenomena*, edited by C. Domb and J. Lebowitz, Vol. 13 (Academic Press, New York, 1989).

[69] P. Adelhardt, J. Gritsch, M. Hille, D. A. Reiss, and K. P. Schmidt, [Phys. Rev. B](#) **96**, 235123 (2017).

Kitaev honeycomb antiferromagnet in a field: quantum phase diagram for general spin Supplementary Material

Saeed S. Jahromi,^{1,2,3} Max Hörmann,⁴ Patrick Adelhardt,⁴
Sebastian Fey,⁴ Román Orús,^{1,5,3} and Kai Phillip Schmidt⁴

¹*Donostia International Physics Center, Paseo Manuel de Lardizabal 4, E-20018 San Sebastián, Spain*

²*Department of Physics, Institute for Advanced Studies in Basic Sciences (IASBS), Zanjan 45137-66731, Iran*

³*Multiverse Computing, Paseo de Miramón 170, E-20014 San Sebastián, Spain*

⁴*Lehrstuhl für Theoretische Physik I, Staudtstraße 7,*

FAU Erlangen-Nuremberg, D-91058 Erlangen, Germany

⁵*Ikerbasque Foundation for Science, Maria Diaz de Haro 3, E-48013 Bilbao, Spain*

The supplementary materials contain details of the tensor-network algorithm as well as of the pCUT method including the explicit series expressions for fixed S and arbitrary S and some information on the extrapolation.

I. TENSOR-NETWORK ALGORITHMS

In this section, we provide the details of the tensor-network (TN) algorithms that have been used for simulating the spin- S Kitaev model on the honeycomb lattice.

A. The iPEPS method for the honeycomb lattice

Exact contraction of an infinite 2D TN is a computationally hard problem. One therefore has to resort to approximation techniques such as tensor renormalization group (TRG) [1, 2] or corner transfer matrix renormalization group (CTMRG) [3–6]. The CTMRG have been proven to be one the most efficient and accurate techniques for contraction of TN with square geometries. Therefore, current state-of-the-art iPEPS algorithms are usually developed for square lattices. In order to simulate other 2D lattice with iPEPS method, one then needs to map the underlying lattice to a square structure. To this end, one can coarse-grain several lattice sites into a square lattice of block-sites [7] or fine-grain [8] the lattice by locally splitting both lattice sites and the corresponding Hilbert space to obtain a square geometry.

Fortunately, the honeycomb lattice already has a rectangular geometry when reshaped into the brick-wall structure. One can then add a dummy link to each site of the lattice to obtain a full square lattice. This mapping is shown in Fig. 1 for the Kitev model on the honeycomb lattice. The corresponding square TN can further be obtained by assigning rank-5 tensors to each site of the lattice given the virtual dimension of the dummy link be set to $D = 1$, as shown in Fig. 2-(a). The resulting TN will then have a square geometry and can be efficiently simulated by the iPEPS code already developed for the square lattice. The only difference is that no Hamiltonian term acts on the trivial index of the two neighboring tensors (see dashed yellow legs in Fig. 2-(a)).

Our iPEPS techniques for both simple update (SU) and full update (FU) is based on the iterative evolution of the Kitev Hamiltonian in imaginary time. The renormalization and truncation of the local tensors are performed by singular-value decomposition for the case of SU and with least-square minimization for the FU. The full environment

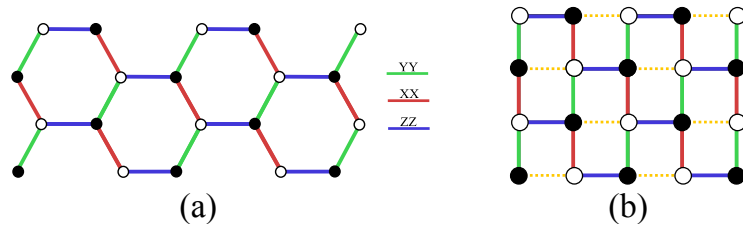


FIG. 1: (Color online) (a) The Kitev model on the honeycomb lattice. (b) Reshaping the honeycomb lattice (a) into the brick-wall structure. By adding dummy links to the lattice, the resulting brick-wall structure will be turned into a square lattice.

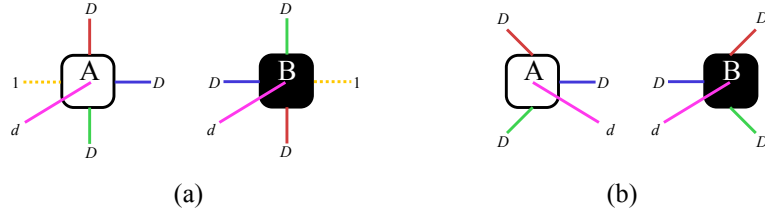


FIG. 2: (Color online) (a) The rank-5 PEPS tensors which are obtained by reshaping the honeycomb lattice into a brick-wall structure and adding dummy indices with dimension $D = 1$ to the tensors. (b) The rank-4 tensors on the original honeycomb lattice which are used in the gPEPS algorithm.

used in the minimization process of the FU as well as the calculation of the expectation values of local operators have been approximated by the CTMRG algorithm.

Within our iPEPS simulations, we managed to push the simulations up to bond dimension $D = 7$ for FU and $D = 11$ for SU. The boundary dimension χ for approximating the environment in the CTMRG was at least $\chi = D^2$. However, we always checked to make sure we are fully converged. Besides, we fixed $\chi = 64$ for $D > 8$.

B. The gPEPS method for any infinite lattice

The gPEPS technique [9], in contrast to the standard iPEPS method which is mostly developed for the square geometry, can be adapted to any lattice geometry and any spatial dimension. The gPEPS algorithm targets the geometrical challenges for TN simulation of local Hamiltonians by resorting to the so-called *structure-matrix* (SM), first proposed by some of the authors in Ref. [9]. Each column of the SM corresponds to one of the links of the lattice and contains all the details about the neighboring tensors, their interconnecting indices, and their bond dimensions. Thanks to this, one can fully automatize the TN update by looping over the columns of the SM in a very systematic way, without the burden of complications due to geometry (see Refs.[9] for detailed discussions).

The gPEPS algorithm uses an optimized version of the SU algorithm for optimizing the TN and further uses a mean-field-like environment for calculating the expectation values of local operators, hence allowing for simulating a larger bond dimension D . Similar to the iPEPS, the gPEPS algorithm is also based on the imaginary-time evolution of the Hamiltonian. The main difference here is that in contrast to the iPEPS in which we mapped the honeycomb lattice to a square TN of rank-5 tensors with one dummy index (Fig. 2-(a)), the gPEPS considers rank-4 tensors (Fig. 2-(b)) in a translationally invariant unit-cell directly on the original honeycomb lattice. The connectivity information of the honeycomb unit-cell used in our gPEPS calculations has been shown for a 8-site unit-cell in Table I.

TABLE I: Structure-matrix of a translationally invariant honeycomb lattice with 8-site unit-cell. The physical dimension of each tensor T_i is labeled by zero. The virtual indices therefore are started from one in each row of the table.

	E_1	E_2	E_3	E_4	E_5	E_6	E_7	E_8	E_9	E_{10}	E_{11}	E_{12}
T_1	1	2	3	0	0	0	0	0	0	0	0	0
T_2	1	0	0	2	3	0	0	0	0	0	0	0
T_3	0	0	0	1	0	2	3	0	0	0	0	0
T_4	0	1	0	0	0	2	0	3	0	0	0	0
T_5	0	0	0	0	1	0	0	0	2	3	0	0
T_6	0	0	1	0	0	0	0	0	2	0	3	0
T_7	0	0	0	0	0	0	1	0	0	2	3	
T_8	0	0	0	0	0	0	1	0	0	2	0	3

We were able to push simulations of the spin- S Kitaev model in the presence of a uniform magnetic field up to $D = 18$ for different S values. The phase boundaries were further detected by calculating different local quantities such as energy and its derivatives, magnetization, nearest-neighbor spin correlation, and Von Neumann bond entanglement entropy as shown in the main text.

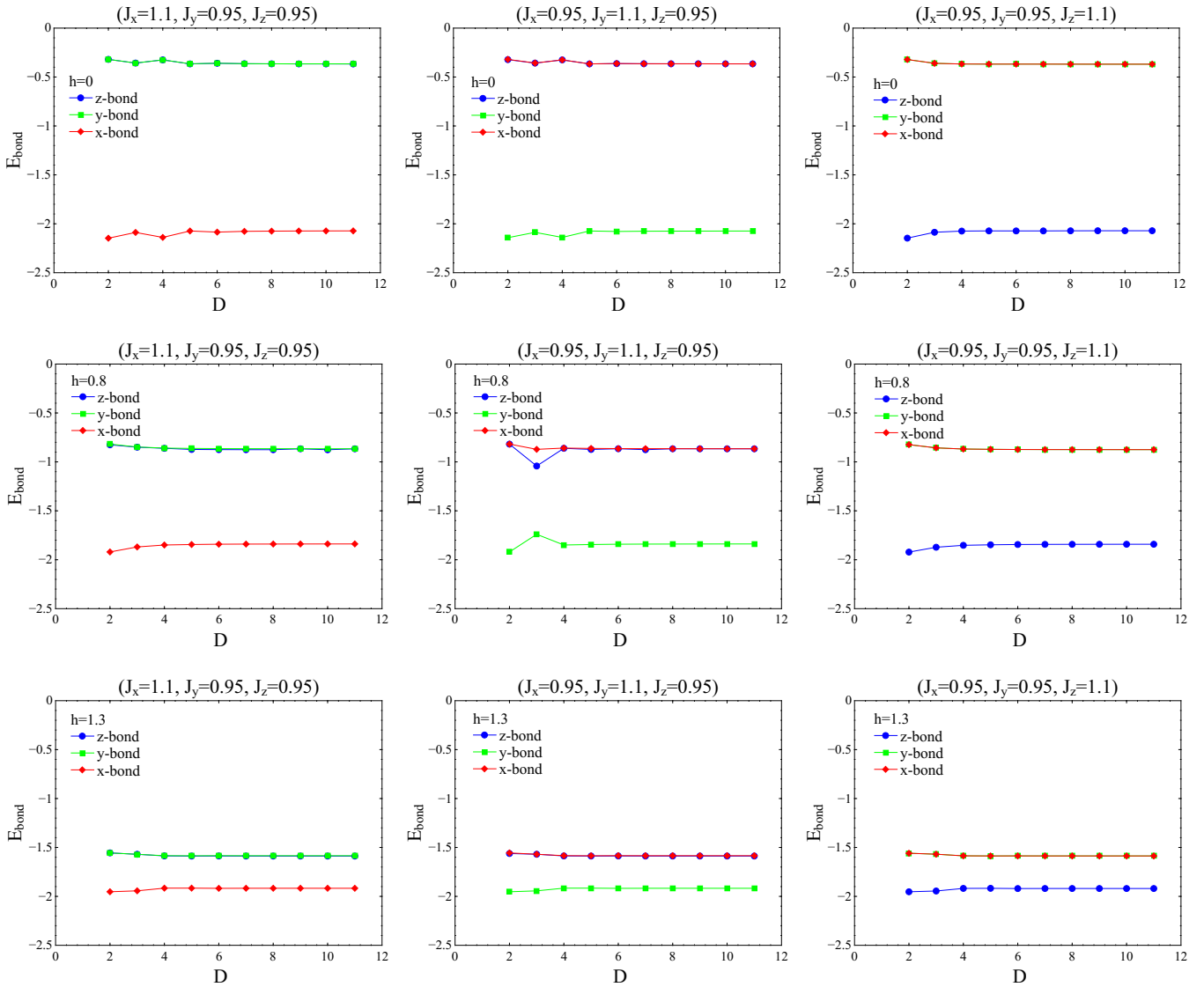


FIG. 3: (Color online) Ground-state energy per-site of the spin-3/2 Kitaev model for different field strength and anisotropic exchange coupling. The bond with larger exchange coupling always has lower energy. As we approach the polarized phase, the bond energies on x -, y - and z -links tend to approach each other until they eventually become fully identical in the polarized phase. Similar results holds for any $S > 1/2$.

C. Tensor-network results for the anisotropic Kitaev model

In order to provide a more clear picture about the nature of different phases in the phase diagram of the antiferromagnetic Kitaev model in a magnetic field, here we present our complimentary results for the anisotropic Kitaev regime, e.g., $(J_x = 1.1, J_y = 0.95, J_z = 0.95)$. Similar to the isotropic case $(J_x = J_y = J_z)$, we observe that by moving slightly away from the isotropic point the bond energies on the x , y , and z -links for $S > 1/2$ become anisotropic and form degenerate patterns with two of the bonds having the same energies while the third one being considerably different, forming dimerized patterns on the honeycomb lattice which are consistent with the semi-classical limit [10]. Fig. 3 demonstrates the bond energies of the spin-3/2 antiferromagnetic Kitaev model for several field strength h and different exchange anisotropies. One can clearly see that the bond with larger exchange coupling always has lower energy. As we approach the polarized phase by increasing the magnetic field, the bond energies on x -, y - and z -bond tend to approach each other until they eventually become fully identical in the polarized phase. Similar results holds for any $S > 1/2$.

II. THE PCUT METHOD

The pCUT method maps the Hamiltonian

$$\mathcal{H}_{\text{KIF}} = J \sum_{\substack{\alpha\text{-links} \\ \alpha=x,y,z \\ <i,j>}} S_i^\alpha S_j^\alpha + h \sum_i (S_i^x + S_i^y + S_i^z) \equiv \mathcal{V} + \mathcal{H}_0, \quad (1)$$

unitarily to an effective Hamiltonian \mathcal{H}_{eff} , which conserves the number of quasi-particles in the polarized high-field phase where spins point in $(1, 1, 1)$ -direction. This mapping is done perturbatively up to high orders in powers of $x \equiv J/h$. The quasi-particles in the polarized phase correspond to dressed spin-flip excitations, which are adiabatically connected to localized spin flips above the fully polarized state in the limit $h \rightarrow \infty$.

It is convenient to perform a local unitary transformation in the spin- S Hamiltonian (1) to a basis, where the field term \mathcal{H}_0 is diagonal. The unperturbed part then reads

$$\mathcal{H}_0 = \sqrt{3}h \sum_i \tilde{S}_i^z, \quad (2)$$

while for the perturbation \mathcal{V} the expression becomes

$$\mathcal{V} = J/6 \sum_{\substack{\gamma\text{-links} \\ \alpha, \beta, \gamma = x, y, z \\ <i,j>}} C_\gamma^{\alpha\beta} \tilde{S}_i^\alpha \tilde{S}_j^\beta. \quad (3)$$

The coefficients $C^{\alpha\beta}$ are given by

$$C_x^{\alpha\beta} = \begin{pmatrix} 1 & \sqrt{3} & -\sqrt{2} \\ \sqrt{3} & 3 & -\sqrt{6} \\ -\sqrt{2} & -\sqrt{6} & 2 \end{pmatrix}, \quad C_y^{\alpha\beta} = \begin{pmatrix} 1 & -\sqrt{3} & -\sqrt{2} \\ -\sqrt{3} & 3 & \sqrt{6} \\ -\sqrt{2} & \sqrt{6} & 2 \end{pmatrix}, \quad C_z^{\alpha\beta} = \begin{pmatrix} 4 & 0 & 2\sqrt{2} \\ 0 & 0 & 0 \\ 2\sqrt{2} & 0 & 2 \end{pmatrix}. \quad (4)$$

The unperturbed part \mathcal{H}_0 has an equidistant spectrum and can therefore be used as a starting point for pCUT. The action of the perturbation depends on the link-type x , y or z but the difference between the three cases only enters in different phase factors. This can be seen from the form of the C -matrices.

We made use of this property to efficiently implement pCUT. For that we employed the white-graph method [11, 12] where we calculated each contribution from a multi-parameter perturbation sequence on graphs tracking all possible phases of the virtual fluctuations. Only after the pCUT calculation was preformed we attributed the right phases, depending on the link types of the graph embedding on the lattice.

A. Ground-state energy and gap

We calculated the ground-state energy and gap up to order 9 in the parameter $x = J/h$ for $S = 1/2$ and up to order 8 for $S = 1$ in units of $\sqrt{3}h$. The series are given by

$$\begin{aligned} \Delta^{S=1/2} = & 0.00000959406432895 x^9 + 0.0000212393084160 x^8 + 0.0000414176411990 x^7 \\ & + 0.0000704746622861 x^6 + 0.000237867694925 x^5 + 0.00111454046639 x^4 \\ & + 0.00801875373874 x^3 + 0.02777777777777 x^2 - 0.577350269189 x + 1.0 , \end{aligned} \quad (5)$$

$$\begin{aligned} \Delta^{S=1} = & 0.0101022918713 x^8 + 0.0115628640647 x^7 + 0.0141008200463 x^6 + 0.0194831516594 x^5 \\ & + 0.0287208504801 x^4 + 0.0481125224324 x^3 + 0.055555555555 x^2 - 1.15470053837 x + 1.0 , \end{aligned} \quad (6)$$

$$\begin{aligned} \varepsilon_0^{S=1/2} = & -0.00000149464455105 x^9 - 0.00000367780870199 x^8 - 0.00000870428476930 x^7 \\ & - 0.0000231117034186 x^6 - 0.0000869246303917 x^5 - 0.000436205353843 x^4 \\ & - 0.00231481481481 x^3 - 0.0120281306081 x^2 + 0.125 x - 0.866025403784 , \end{aligned} \quad (7)$$

and

$$\begin{aligned}\varepsilon_0^{S=1} = & -0.00294477723047 x^8 - 0.00390784623983 x^7 - 0.00543115959436 x^6 \\ & - 0.00806374790428 x^5 - 0.0129933509655 x^4 - 0.0231481481481 x^3 \\ & - 0.0481125224324 x^2 + 0.5 x - 1.73205080756 .\end{aligned}\quad (8)$$

B. Observable

Furthermore we have calculated the spectral weight of the gap mode $|\Delta^S\rangle$ measured by the Fourier transform of the observable $\mathcal{O}_i \equiv S_i^z$, $\mathcal{O}_{\text{Gap}} = \frac{1}{\sqrt{2N_u}} \sum_{i,j} \sum_{\alpha=0}^1 (-1)^\alpha \mathcal{O}_{i,j,\alpha}$, which reads

$$A_{\text{Gap}}^S \equiv |\langle \text{ref} | \mathcal{O}_{\text{Gap}}^{\text{eff}} | \Delta^S \rangle|^2 . \quad (9)$$

Here i, j represent the coordinate of the unit cell, α the position in the unit cell and N_u is the number of unit cells. The observable thus has the same phase factors as the gap mode. The unitary transformation of pCUT is used to transform \mathcal{O}_{Gap} to $\mathcal{O}_{\text{Gap}}^{\text{eff}}$. For $S = 1/2$ it is given up to order 8 by

$$\begin{aligned}A_{\text{Gap}}^{S=1/2} = & -0.0000447670776607 x^8 - 0.0000874502157678 x^7 - 0.000206177711284 x^6 \\ & - 0.000531879498960 x^5 - 0.00220407521719 x^4 - 0.00534583582582 x^3 - 0.0138888888888 x^2 + 1.0 .\end{aligned}\quad (10)$$

III. HIGH-FIELD PCUT EXPANSION FOR GENERAL SPIN S

A. Ground-state energy and gap

The goal is to obtain the ground-state energy per site ε_0 and the gap Δ as a function of $x = J/h$ for a general spin value S in units of $\sqrt{3}h$. While for fixed spin values this is performed regularly with the pCUT method, deducing linked-cluster expansion for general S has not been done to the best of our knowledge. Consequently, we will describe this part in more detail in the following. For that purpose it is instructive to write down the general action of \tilde{S}^x - and \tilde{S}^y -operators in the eigenbasis $|m\rangle$ with $m \in \{-S, \dots, +S\}$ of the \tilde{S}^z -operator,

$$\begin{aligned}\langle m' | \tilde{S}^x | m \rangle &= \frac{1}{2} \sqrt{S(S+1) - m'm} (\delta_{m',m+1} + \delta_{m'+1,m}) \\ \langle m' | \tilde{S}^y | m \rangle &= \frac{1}{2i} \sqrt{S(S+1) - m'm} (\delta_{m',m+1} - \delta_{m'+1,m}) \\ \langle m' | \tilde{S}^z | m \rangle &= m \delta_{m',m} .\end{aligned}\quad (11)$$

In the following we describe our approach for the ground-state energy ε_0 . Contributions in the perturbative expansion correspond to virtual fluctuations. In the case of ε_0 the amplitudes of these fluctuations are given by expectation values with respect to the reference state $| -S - S \dots - S \rangle$. In order k perturbation theory the expectation values then involve operator sequences containing k -times the perturbation \mathcal{V} . Obviously, for terms in \mathcal{V} containing solely spin operators \tilde{S}^x and \tilde{S}^y , one only gets a finite contribution to ε_0 in order k perturbation theory if each site has been acted on an even number of times. As a consequence, the final contribution will be a polynomial in S of order k , since the square-root expressions in Eq. (11) for matrix elements from m to m' will always occur with an even multiplicity. Further, for the term proportional to $\tilde{S}^z \tilde{S}^z$, one has to note that the constant contribution $\propto S^2$ is not part of the perturbation \mathcal{V} since it is just a constant times the identity matrix. The leading term is therefore proportional to S . Finally, for $\tilde{S}^x \tilde{S}^z$, the contribution proportional to $(-S)\sqrt{S}$ is zero because of destructive interferences of the three Kitaev links on each vertex. Here the leading term is proportional to \sqrt{S} . Altogether, each term in \mathcal{V} scales at most with S so that in order k perturbation theory one obtains a polynomial of order k in S .

Thus one way to calculate the general S contribution to the ground-state energy ε_0 is to perform the calculation for a sufficiently large number of S -values allowing to determine the polynomial in S exactly. Instead of doing this we applied a more efficient approach described in the following. We introduce three perturbation parameters to distinguish contributions of order S , \sqrt{S} , and 1. This way only a single calculation has to be performed. Further,

the maximal local Hilbert space needed is only of dimension $\lfloor k/2 \rfloor$ in contrast to $k+1$ that one needs for the naive approach. We then exploit that

$$\begin{aligned} \sqrt{S(S+1) - (-S+d)(-S+d+1)}^2 &= 2(d+1)S - d(d+1) \\ &= (\sqrt{2(d+1)S} - \sqrt{d(d+1)})(\sqrt{2(d+1)S} + \sqrt{d(d+1)}) \quad . \end{aligned} \quad (12)$$

Whenever a spin operator \tilde{S}^x or \tilde{S}^y acts and increases the eigenvalue of \tilde{S}^z , we assign to the corresponding spin operator the factor $(\sqrt{2(d+1)S} + \sqrt{d(d+1)})$. In contrast, if the eigenvalue of \tilde{S}_z decreases, we track the factor $(\sqrt{2(d+1)S} - \sqrt{d(d+1)})$. This way each action of \mathcal{V} can be decomposed into contributions proportional to S , \sqrt{S} , and 1. This explains how $\tilde{S}^x \tilde{S}^x$ -, $\tilde{S}^x \tilde{S}^y$ - and $\tilde{S}^y \tilde{S}^y$ -processes have to be treated. All other terms can be handled in a similar manner straightforwardly.

In practice, we have calculated the ground-state energy for general values of S up to order 7 in x . Up to order 4, this expression reads

$$\begin{aligned} \varepsilon_0^S &= (-0.0191559117092 S^4 + 0.00623680846346 S^3 - 0.0000742477198031 S^2) x^4 \\ &\quad + (-0.02777777777777 S^3 + 0.00462962962962 S^2) x^3 - 0.0481125224324 S^2 x^2 \\ &\quad + 0.5 S^2 x - 1.73205080756 S \quad . \end{aligned} \quad (13)$$

Note that the general expression agrees with the expressions in Eq. (7) and Eq. (8) for $S = 1/2$ and $S = 1$. Further, for $S \in \{\frac{3}{2}, 2\}$, the series expansions read

$$\begin{aligned} \varepsilon_0^{S=3/2} &= -0.0949621005193 x^7 - 0.0829288164821 x^6 - 0.0766192986968 x^5 \\ &\quad - 0.0760946318332 x^4 - 0.0833333333333 x^3 - 0.108253175473 x^2 \\ &\quad + 1.125 x - 2.59807621135 \\ \varepsilon_0^{S=2} &= -0.841028333911 x^7 - 0.533302274710 x^6 - 0.357243560432 x^5 \\ &\quad - 0.256897110519 x^4 - 0.203703703703 x^3 - 0.192450089729 x^2 \\ &\quad + 2.0 x - 3.46410161513 \quad . \end{aligned} \quad (14)$$

The same approach can also be realized for the one-particle gap Δ and we also have reached order 7 for general values of S . Up to order 4, this expression reads

$$\begin{aligned} \Delta^S &= (0.00437242798353 S - 0.0329218106995 S^2 + 0.0572702331961 S^3) x^4 \\ &\quad + (0.0641500299099 S^2 - 0.0160375074774 S) x^3 + 0.0555555555555 S x^2 \\ &\quad - 1.15470053837 S x + 1 \quad . \end{aligned} \quad (15)$$

The general expression here also agrees with the expressions in Eq. (5) and Eq. (6) for $S = 1/2$ and $S = 1$. Further, for $S \in \{1, \frac{3}{2}, 2\}$, the series expansions read

$$\begin{aligned} \Delta^{S=1} &= 0.0101022918713 x^8 + 0.0115628640647 x^7 + 0.0141008200463 x^6 + 0.0194831516594 x^5 \\ &\quad + 0.0287208504801 x^4 + 0.0481125224324 x^3 + 0.0555555555555 x^2 - 1.15470053837 x + 1.0 \\ \Delta^{S=3/2} &= 0.217999872570 x^7 + 0.170528114759 x^6 + 0.143725023609 x^5 + 0.125771604938 x^4 \\ &\quad + 0.120281306081 x^3 + 0.0833333333333 x^2 - 1.73205080756 x + 1.0 \\ \Delta^{S=2} &= 1.57595243639 x^7 + 0.895840698332 x^6 + 0.539783672884 x^5 + 0.335219478737 x^4 \\ &\quad + 0.224525104684 x^3 + 0.111111111111 x^2 - 2.30940107675 x + 1.0 \quad . \end{aligned} \quad (16)$$

B. Dispersion

Using the full graph decomposition we do not only have information about the energy gap but also about the complete one-particle spectrum. There are two atoms per unit cell which yields two bands after diagonalization via Fourier transform. The two dispersions in second order in x for general S are

$$1 - S/\sqrt{3}x + (4/27)((S^2 \cos(k_x - k_y))/8 - (3S)/8 - (3S^2)/8 + (S^2 \cos(k_x))/8 + (S^2 \cos(k_y))/8)x^2 \pm Sx(2x/(3\sqrt{3}) - 2)/(6\sqrt{3})\sqrt{2 \cos(k_x - k_y) + 2 \cos(k_x) + 2 \cos(k_y) + 3}. \quad (17)$$

C. Observable

In principle the calculation of the local observable $\mathcal{O}_i \equiv S_i^z$ for general S is performed by the same technique.

Special care has to be taken when implementing the action of the observable. One again has to distinguish between observable processes that increase or decrease the \tilde{S}^z -value.

This means, e.g., for the \tilde{S}^x -part of S^z one has to distinguish behaviour where \tilde{S}^x increases the \tilde{S}^z -value by one and attribute $(\sqrt{2(d+1)S} + \sqrt{d(d+1)})$ to it while for processes where the \tilde{S}^z -value gets decreased by one one has to use $(\sqrt{2(d+1)S} - \sqrt{d(d+1)})$ instead.

We have calculated the effective observable $\mathcal{O}_i^{\text{eff}}$ for general values of S up to order 6 in $x = J/h$. Up to order 4, this expression reads

$$A_{\text{Gap}}^S = (0.00167181069958 S^2 + 0.0155178326474 S^3 - 0.0729881115683 S^4) x^4 + (0.0106916716516 S^2 - 0.0641500299099 S^3) x^3 - 0.0555555555555 S^2 x^2 + 2.0 S. \quad (18)$$

The general expression agrees with the expression in Eq. (10) for $S = 1/2$. Further, for $S \in \{1, \frac{3}{2}, 2\}$, the series expansions read

$$\begin{aligned} A_{\text{Gap}}^{S=1} &= -0.000131804332821 x^6 - 0.000393123245477 x^5 - 0.00122465773873 x^4 \\ &\quad - 0.00304831580551 x^3 - 0.00823045267489 x^2 + 2.0 \\ A_{\text{Gap}}^{S=3/2} &= -0.00191804537762 x^6 - 0.00359256457652 x^5 - 0.00687776253619 x^4 \\ &\quad - 0.0109739368998 x^3 - 0.0185185185185 x^2 + 3.0 \\ A_{\text{Gap}}^{S=2} &= -0.0119676532972 x^6 - 0.0163624232067 x^5 - 0.0227595035635 x^4 \\ &\quad - 0.0268251790885 x^3 - 0.0329218106995 x^2 + 4.0. \end{aligned} \quad (19)$$

IV. EXTRAPOLATION

Extrapolation techniques like Padé and DLog Padé approximation are the most common techniques to extrapolate high-order series. For a general introduction we refer to Ref. [13]. The Padé approximant of order $[L, M]$ is given by

$$P[L, M] = \frac{P_L(x)}{Q_M(x)} = \frac{p_0 + p_1 x + \cdots + p_L x^L}{1 + q_1 x + \cdots + q_M x^M} \quad (20)$$

where the coefficients p_i and q_i are given uniquely by the requirement that the Taylor series of $P[L, M]$ in the expansion parameter x up to order $L + M$ must correspond to the calculated series F of the same order. Further, DLog Padé approximants $dP[L, M]$ correspond to a Padé approximation of the logarithmic derivative

$$D(x) = \frac{d}{dx} \ln(F(x)) \quad . \quad (21)$$

[1] M. Levin and C. P. Nave, *Physical Review Letters* **99**, 120601 (2007), arXiv:0611687 [cond-mat].
[2] Z. C. Gu, M. Levin, and X. G. Wen, *Physical Review B - Condensed Matter and Materials Physics* **78**, 205116 (2008), arXiv:0807.2010 .
[3] T. Nishino and K. Okunishi, *Journal of the Physical Society of Japan* **65**, 891 (1996), arXiv:9507087 [cond-mat].
[4] R. Orús and G. Vidal, *Physical Review B - Condensed Matter and Materials Physics* **80**, 094403 (2009), arXiv:0905.3225 .

- [5] P. Corboz, T. M. Rice, and M. Troyer, *Physical Review Letters* **113**, 046402 (2014), arXiv:1402.2859 .
- [6] P. Corboz, J. Jordan, and G. Vidal, *Physical Review B - Condensed Matter and Materials Physics* **82**, 245119 (2010), arXiv:1008.3937 .
- [7] S. S. Jahromi, R. Orús, M. Kargarian, and A. Langari, *Physical Review B* **97**, 115161 (2018).
- [8] P. Schmoll, S. S. Jahromi, M. Hörmann, M. Mühlhauser, K. P. Schmidt, and R. Orús, *Physical Review Letters* **124**, 200603 (2020), arXiv:1911.04882 .
- [9] S. S. Jahromi and R. Orús, *Physical Review B* **99**, 195105 (2019).
- [10] I. Rousochatzakis, Y. Sizuk, and N. B. Perkins, *Nature Communications* **9**, 1575 (2018).
- [11] K. Coester and K. P. Schmidt, *Physical Review E* **92**, 22118 (2015).
- [12] P. Adelhardt, J. A. Koziol, A. Schellenberger, and K. P. Schmidt, *Phys. Rev. B* **102**, 174424 (2020).
- [13] A. C. Guttmann, *Phase Transitions and Critical Phenomena*, edited by C. Domb and J. Lebowitz, Vol. 13 (Academic Press, New York, 1989).